

Ultrastrong Magnon-Photon Coupling Achieved by Magnetic Films in Contact with Superconducting Resonators

Alberto Ghirri^{1,*}, Claudio Bonizzoni^{2,1}, Maksut Maksutoglu³, Alberto Mercurio⁴,
Omar Di Stefano⁴, Salvatore Savasta⁴ and Marco Affronte^{1,2,1}

¹ Istituto Nanoscienze—CNR, Centro S3, via G. Campi 213/A, Modena 41125, Italy

² Dipartimento di Scienze Fisiche, Informatiche e Matematiche, Università di Modena e Reggio Emilia, via G. Campi 213/A, Modena 41125, Italy

³ Institute of Nanotechnology, Gebze Technical University, Gebze, Kocaeli 41400, Turkey

⁴ Dipartimento di Scienze Matematiche e Informatiche, Scienze Fisiche e Scienze della Terra, Università di Messina, Messina 98166, Italy

(Received 2 February 2023; revised 26 June 2023; accepted 21 July 2023; published 16 August 2023)

Coherent coupling between spin-wave excitations (magnons) and microwave photons in a cavity may disclose new paths to unconventional phenomena as well as novel applications. Here, we present a systematic investigation of yttrium iron garnets (YIG) films on top of coplanar waveguide resonators made of superconducting $\text{YBa}_2\text{Cu}_3\text{O}_7$ (YBCO). We first show that spin-wave excitations with frequency higher than the Kittel mode can be excited by putting in direct contact a 5- μm -thick YIG film with the YBCO coplanar resonator (cavity frequency $\omega_c/2\pi = 8.65$ GHz). With this configuration, we obtain very large values of the collective coupling strength $\lambda/2\pi \approx 2$ GHz and cooperativity $C = 5 \times 10^4$. Transmission spectra are analyzed by a modified Hopfield model for which we provide an exact solution that allows us to well reproduce spectra by introducing a limited number of free parameters. It turns out that the coupling of the dominant magnon mode with photons exceeds 0.2 times the cavity frequency, thus demonstrating the achievement of the ultrastrong-coupling regime with this architecture. Our analysis also shows a vanishing contribution of the diamagnetic term, which is a peculiarity of pure spin systems.

DOI: 10.1103/PhysRevApplied.20.024039

I. INTRODUCTION

The interplay between magnetic excitations and electromagnetic radiation has recently assumed a pivotal role in many fields of research such as magnonics, spintronics, magneto-optomechanics, and information processing for its potentialities in the development of hybrid systems and devices [1–4]. The control of magnon-photon coupling and cooperativity is one of the keys for enabling the exploitation of unique functionalities related to the coherent dynamics in these systems. Novel applications, including memory devices [5], coherent spin pumping [6], haloscopes for axion detection [7], microwave-optical transducers [8], and coherent microwave sources [9], have already been tested. An open issue is the realization of all-on-chip devices for their efficient integration in microwave circuits [4].

In the prototypical case of a ferromagnetic sample embedded in a microwave resonator, spin waves couple

with resonant electromagnetic modes [10] and the system can be modeled by combining Maxwell and Landau-Lifshitz-Gilbert equations [11,12]. This classical description works remarkably well in the case of the ferrimagnetic yttrium iron garnet (YIG) [3], which has been studied in detail, showing a combination of several optimal features, including the exceptionally low damping of magnetization precession [13].

In the quantum regime, spin waves are collective (bosonic) excitations (magnons) that may coherently interact with cavity photons [14,15]. The Dicke model and its evolution in the Hopfield version which also includes the diamagnetic term, have been developed to describe a large variety of hybrid light-matter quantum systems [16,17]. In the strong-coupling regime, the rotating-wave approximation (RWA) and the (Jaynes-) Tavis-Cummings Hamiltonian have been mainly used to interpret the experimental data [3]. However, there is a general trend now to push these studies beyond conventional coupling regimes and more specifically to reach coupling strengths, λ , that are a non-negligible fraction of the cavity frequency, ω_c . Under these conditions, novel effects related to processes that do not conserve the number of excitations in the system

* alberto.ghirri@nano.cnr.it

have been predicted [16,17]. For $\lambda/\omega_c \geq 0.1$, we refer to the ultrastrong-coupling (USC) regime, in which counter-rotating terms, neglected in the RWA, must be considered. In this context, the description of the fundamental interaction between the electromagnetic field and the magnetic system, including the diamagnetic term, which plays a key role in the super-radiant phase transition [18–21], still needs to be clarified and tested on real magnetic materials.

A few experimental reports show magnetic systems achieving the USC regime with microwave resonators. The USC regime was first reported in the case of millimeter-size YIG crystals in three-dimensional (3D) cavities [22–26] and a few other magnetic materials [27–30]. In view of the realization of scalable architectures, small magnets coupled to superconducting planar resonant geometries have recently been designed and observed to achieve the (ultra)strong-coupling regime [31–38]. In spite of these encouraging results, the optimization of these hybrid systems for the USC regime is still largely unexplored. For instance, the geometry of the hybrid superconductor-magnet system needs to be optimized in order to maximize their mutual coupling, while magnetic materials may be preferably insulating in order to minimize the damping. Moreover, the vicinity to a superconducting material, which has to be resilient to magnetic fields [39] to allow for ferromagnetic resonance (FMR) experiments, may significantly affect the spectrum of magnetic excitations through several mechanisms [34,40].

In this paper, we address the problem of reaching the USC regime in coupled superconductor-ferrimagnet hybrid architectures. By means of a series of systematic experiments carried out with YIG films and planar transmission-line resonators, we demonstrate the achievement of high coupling rates by positioning the magnetic film in direct contact with the superconducting resonator. In our geometry, the excitation of spin waves takes place at the superconductor-ferrimagnet interface, where the amplitude of the microwave field is maximum. The optimized magnon-photon coupling results in collective coupling strengths as large as 0.2 times the cavity frequency. Data analysis, carried out with a modified Hopfield model for which we provide an exact solution, also evidences vanishingly small diamagnetic coupling for magnon excitations in YIG.

The paper is organized as follows. We start by presenting the experimental methods in Sec. II, whilst in Sec. III we report numerical simulations of the profile of the oscillating field which allow us to estimate the volume and coupling strength involved in the spin-photon process. Experimental results are presented in a progressive way by considering the broadband characterization first in Sec. IV, and then transmission spectra on resonators in Sec. V. Modeling and data analysis are reported in Sec. VI, then discussion and concluding remarks in the last two sections. Some appendices follow.

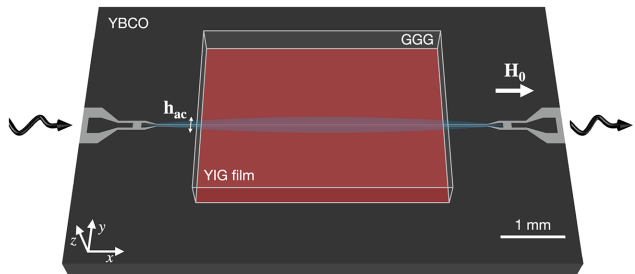


FIG. 1. Sketch of the YBCO/sapphire CPW resonator with the YIG/GGG film positioned above.

II. EXPERIMENTAL METHODS

To study the coupling with different YIG samples, we prepared planar resonators with different sizes and geometries, including meanders with multiple resonance frequencies and inverse anapole resonators with focused electromagnetic radiation [41]. Here we report on two types of planar devices: microstrip and coplanar waveguide (CPW) resonator (Fig. 1). For each of them, the corresponding broadband transmission line, having the same dimensions and geometry (except for the presence of the input and output coupling gaps defining the half-wavelength resonator), has been fabricated to investigate the spin-wave excitation spectrum in the different cases. Microstrip lines having 500- μm -wide central strips were obtained by wet etching of Ag/Al₂O₃ films [42]. Superconducting CPW lines (Fig. 1) were fabricated from commercial YBa₂Cu₃O₇ (YBCO) films deposited on sapphire. Etching was carried out by Ar plasma in a reactive ion etching chamber. The central conductor had length $l \approx 6$ mm, width $w = (17 \pm 1)$ μm , and separation $s = (14 \pm 1)$ μm from the lateral ground planes. Further details are given in Ref. [43].

The experiments were carried out at low temperature in an applied magnetic field (\mathbf{H}_0), which was oriented in the plane of the film along x (Fig. 1). Frequency-swept spectra were acquired using a Vector Network Analyzer with typical incident power $P_{\text{inc}} = -8$ dBm. We studied YIG films grown by liquid-phase epitaxy on 500- μm -thick gadolinium gallium garnet (GGG) substrates. Unless otherwise specified, the film has rectangular shape with a thickness of 5 μm and in-plane size of 4×3 mm². The sample was mounted in diverse ways on the aforementioned microwave transmission lines and resonators. We anticipate that different spin-wave spectra and, ultimately, different magnon-photon coupling strengths were obtained in different cases. In the following we thus consider three experimental configurations: YIG film glued on metallic microstrip (case A); YIG film glued on YBCO CPW line (case B); and YIG film in contact with the YBCO CPW line (case C). In cases A and B the estimated film-resonator separation was on the order of 10 μm . In case C we obtained a good contact between YBCO and YIG surfaces

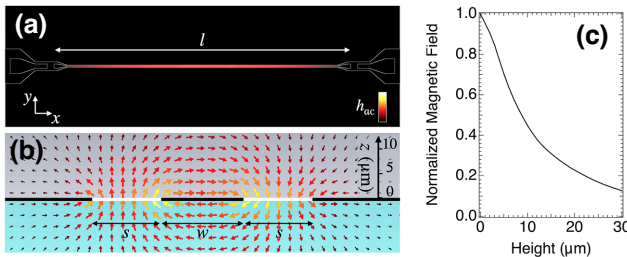


FIG. 2. Calculated profile of the oscillating field (magnetic component) for the fundamental mode of the bare CPW resonator. (a) Top view of the distribution $h_{ac}(x, y, z = 0)$ showing the magnetic antinode in the middle of the resonator. (b) Profile of h_{ac} (phase = 0) in the plane perpendicular to the x direction. The x component of h_{ac} is vanishingly small. (c) Mean value of $h_{ac}(z)$ plotted as a function of the z height.

thanks to a polytetrafluoroethylene (PTFE) screw that gently pushed the GGG substrate against the YBCO surface from the backside.

III. ELECTROMAGNETIC SIMULATIONS

Finite-element electromagnetic simulations were carried out using commercial software to evaluate the amplitude and distribution of the resonator fields. The maps calculated for the CPW resonator [Figs. 2(a) and 2(b)] show the expected in-plane and out-of-plane profiles of the microwave magnetic field, \mathbf{h}_{ac} . The resonator field is mostly confined around the central line between the lateral ground planes, in a region of approximate width $w + 2s = 45 \mu\text{m}$ [43]. To evaluate the z dependence of the resonator field, we calculated the in-plane averaged value of h_{ac} as a function of the z height [Fig. 2(c)]. The decay of $h_{ac}(z)$ is quasieponential and for $z = 10 \mu\text{m}$ it results in a reduction of a factor ≈ 2 with respect to the maximum value.

We can exploit these electromagnetic simulations to estimate the amplitude of the vacuum fluctuation b_{vac} and, consequently, the spin-photon coupling strength (g_s) expected with this particular CPW resonator. By rescaling the calculated magnetic field to the single-photon power level [43], we obtain $b_{\text{vac}} \approx 3 \text{ nT}$. This value is in perfect agreement with the value derived from $b_{\text{vac}} \approx (\mu_0 \omega_c / 4w) \sqrt{\hbar / Z_0}$ [31,44], where $\hbar = 6.626 \times 10^{-34} \text{ J s}$ is the Planck constant and $Z_0 = 58 \Omega$ is the nominal impedance of the CPW resonator. The spin-photon coupling strength then results as $g_s = \gamma b_{\text{vac}} / 4 = 21 \text{ Hz}$, where $\gamma = 28.02 \text{ GHz/T}$ is the electron's gyromagnetic ratio. For comparison, the value of the spin-photon coupling expected for the fundamental mode of the microstrip resonator is less than 1 Hz.

IV. BROADBAND TRANSMISSION SPECTROSCOPY CHARACTERIZATION

We first present a series of transmission (S_{21}) spectra obtained with broadband transmission lines by sweeping the microwave frequency (ω) at steady values of the external magnetic field H_0 (Fig. 3). In the case of the microstrip (case A), the main resonance dip follows the Kittel relation [Fig. 3(a)], which, for in-plane magnetized films, reduces to [45]

$$\omega_{\text{FMR}} = \sqrt{\omega_H(\omega_H + \omega_M)}, \quad (1)$$

where $\omega_H/2\pi = \gamma \mu_0 H_0$ and $\omega_M/2\pi = \gamma \mu_0 M_s$, with $\mu_0 = 4\pi \times 10^{-7} \text{ H/m}$ being the vacuum permeability and $\mu_0 M_s = 0.245 \text{ T}$ the saturation magnetization of YIG as reported in the literature [13,43].

For case B, the numerical derivative of the signal $\partial S_{21}(\omega, H_0) / \partial H_0$ is shown in Fig. 3(b). Additional spin-wave resonance modes are clearly visible in this case. Such modes are commonly observed for YIG films [46,47] but their frequency specifically depends on the profile of the microwave field \mathbf{h}_{ac} . In particular, narrow CPW lines efficiently excite traveling spin waves with finite wave vector $0 < k \leq 2\pi/s$ [48]. Given the in-plane magnetization of the film ($\mathbf{H}_0 \parallel x$) and the negligible x component of \mathbf{h}_{ac} (Fig. 2), the dispersion of the Damon-Eshbach modes follows the characteristic expression [12]

$$\omega_{\text{DE}} = \sqrt{\left(\omega_H + \frac{\omega_M}{2}\right)^2 - \left(\frac{\omega_M}{2}\right)^2 e^{-2kd}}, \quad (2)$$

where $k = k_s = 2\pi/s = 4.5 \times 10^5 \text{ rad/m}$ [dashed-dotted line in Fig. 3(b)] [49]. We note that ω_{DE} is near the maximum limit of Eq. (2), $\omega_H(H_0) + \omega_M/2$, whilst the coupling between the magnetization of YIG and GGG [50] is not evident from the measured spectra [43].

Figure 3(c) displays the spectrum obtained in case C. Here the transmission spectrum shows several additional spin-wave modes whose origin can be related to the special boundary conditions imposed by the contact of the magnetic YIG with the superconducting YBCO planes, as observed in similar experiments [51,52]. Such modes are located in a wide absorption band between $\omega_{\text{DE}}(H_0)$ and $\omega_H(H_0) + \omega_M$, and their typical linewidth is $10 \lesssim \kappa_m \lesssim 40 \text{ MHz}$.

V. ENHANCED SPIN-PHOTON COUPLING AND COOPERATIVITY

Once we had identified the main features of the spin-wave excitation spectrum, we performed experiments in a similar configuration, with the YIG film on half-wavelength resonators having dimensions and geometries equivalent to those of the broadband lines used in Fig. 3 [43]. The S_{21} map taken with the microstrip resonator (case

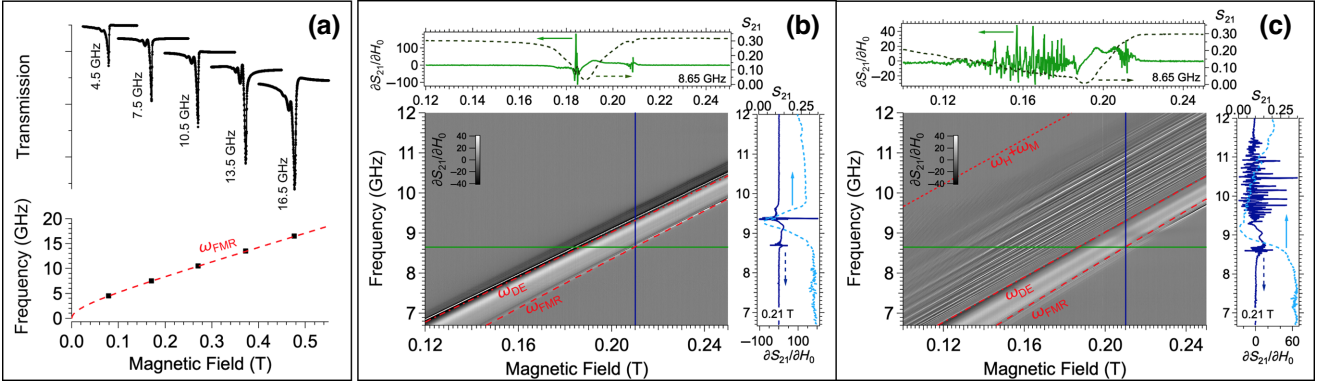


FIG. 3. Broadband characterization of the YIG film. (a) Ag/alumina microstrip, case A. Top: field-swept transmission spectra (temperature $T = 50$ K), taken at different continuous-wave frequencies, as indicated. Bottom: plot of the excitation frequencies as a function of the measured resonance field; the dashed line shows the fit with Eq. (1). (b) YBCO/sapphire CPW line, case B ($T = 30$ K). Center: spectral map showing $\partial S_{21}(\omega, H_0)/\partial H_0$ (arbitrary units). Top: plot of S_{21} and $\partial S_{21}/\partial H_0$ as functions of H_0 for $\omega/2\pi = 8.65$ GHz. Right: plot of S_{21} and $\partial S_{21}/\partial H_0$ as functions of ω for $H_0 = 0.21$ T. (c) Same as panel (b) with YIG in contact with the CPW line, case C.

A) is shown in Fig. 4(a). The lower branch has an oblique asymptote with the FMR mode [Eq. (1)], while the upper branch is barely visible owing to multiple resonances with spin-wave modes. This situation is common with other spin ensemble [53,54] or YIG [3] systems in a resonator mode. From Fig. 4(a) the collective coupling strength can be roughly estimated to be of order of hundreds of megahertz.

The YBCO CPW resonator has, with respect to the microstrip, a smaller mode volume that results in a larger spin-photon coupling g_s (Sec. III). A large anticrossing, having well-defined polariton branches, is obtained in this case [case B, Fig. 4(b)]. Even larger couplings were obtained when the YIG film was put in direct contact with the YBCO resonator (case C): with this geometry, the splitting rises to $2\lambda/2\pi \approx 4$ GHz [Fig. 4(c)], a factor of ≈ 2 larger than in case B. Within the anticrossing gap, no additional modes are visible except for ω_{FMR} . This suggests that this mode is weakly coupled to the CPW resonator. Additional spin-wave excitations are observed above ≈ 10 GHz due to the presence of a spurious box mode [Figs. 4(b) and 4(c)].

It is worth estimating the cooperativity, which is commonly defined as $C = 4\lambda^2/(\kappa_m\kappa_c)$ [17]. From our spectra we take $\kappa_m/2\pi = 40$ MHz and $\kappa_c/2\pi = 8$ MHz as decay rates of magnon (Sec. IV) and uncoupled cavity [43] modes. With these numbers, we achieve $C = 5 \times 10^4$. Considering the normalized parameter $U = \sqrt{(4\lambda^2/\kappa_m\kappa_c)(\lambda/\omega_c)} = 108$, we infer that our results ranks among the best-performing physical platforms for the reaching of the USC regime [17].

VI. SYSTEM HAMILTONIAN

We model our system by considering a quantized single-mode electromagnetic field (with ω_c cavity frequency)

interacting with an ensemble of magnetic moments. We consider collective operators for the spin ensemble, the quantization of both spin excitations and the electromagnetic field, which allows us to introduce the respective bosonic operators \hat{a} and \hat{b} . Because of the vanishing orbital angular momentum of Fe^{3+} in YIG [12], we expect a prominent Zeeman interaction of the type $\hat{\mathcal{H}}_Z = -g_e\hat{\sigma} \cdot \mu_B \hat{\mathbf{h}}$ for a single spin. Here $[\hat{\sigma}_j, \hat{\sigma}_k] = i\epsilon_{jkl}\hat{\sigma}_l$ are the Pauli operators, $\hat{\mathbf{h}}$ is the magnetic field component of the cavity resonator, while μ_B is the Bohr magneton and $g_e \approx 2$ in the case of a simple electron. However, so as not to exclude the possibility of having orbital angular momentum contributions in our hybrid system, we also consider this degree of freedom including a diamagnetic term, which comes from the usual minimal coupling replacement.

The total Hamiltonian then reads ($\hbar = 1$)

$$\begin{aligned} \hat{\mathcal{H}} = & \omega_c \hat{a}^\dagger \hat{a} + \frac{\omega_b}{2} \sum_{j=1}^N \sigma_z^{(j)} + \frac{\lambda}{2\sqrt{N}} \sum_{j=1}^N \sigma_x^{(j)} (\hat{a} + \hat{a}^\dagger) \\ & + \beta (\hat{a} + \hat{a}^\dagger)^2, \end{aligned} \quad (3)$$

where \hat{a} (\hat{a}^\dagger) is the photon annihilation (creation) operator, ω_c is the cavity resonance frequency, ω_b is the resonance frequency of a single spin, λ is the collective light-matter coupling, and β is the coefficient of the diamagnetic term.

By using the collective spin operators $\hat{J}_z \equiv (1/2) \sum_{j=1}^N \hat{\sigma}_z^{(j)}$ and $\hat{J}_x = \hat{J}_+ + \hat{J}_- \equiv (1/2) \sum_{j=1}^N \hat{\sigma}_x^{(j)}$, we can apply the Holstein-Primakoff transformations [55]

$$\hat{J}_z \rightarrow \hat{b}^\dagger \hat{b} - \frac{N}{2}, \quad \hat{J}_+ \rightarrow \hat{b}^\dagger \sqrt{N - \hat{b}^\dagger \hat{b}}, \quad \hat{J}_- = \hat{J}_+^\dagger, \quad (4)$$

where \hat{b} and \hat{b}^\dagger are the magnon annihilation and creation operators, respectively, which obey the standard bosonic

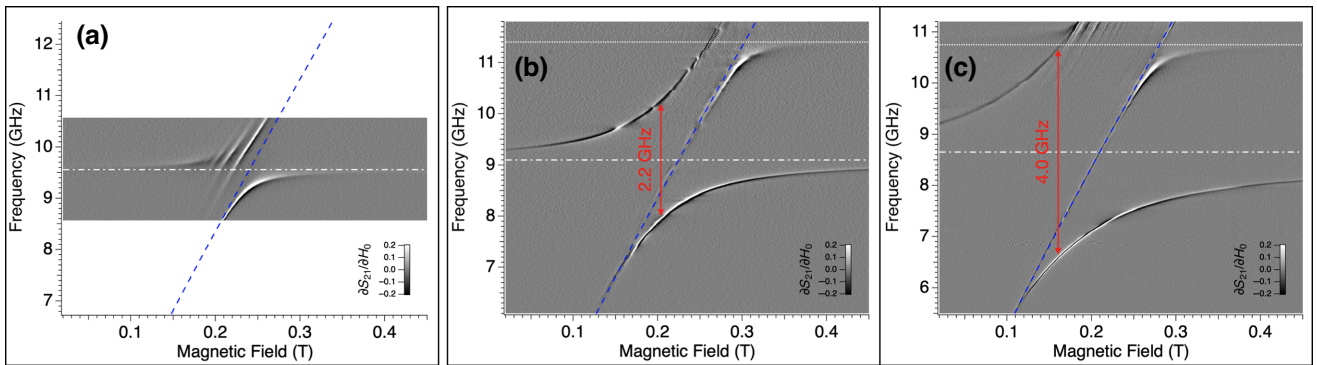


FIG. 4. Coupling of the YIG film with different planar resonators ($P_{\text{inc}} = -8 \text{ dBm}$): (a) microstrip resonator, case A ($T = 50 \text{ K}$); (b) CPW resonator, case B ($T = 30 \text{ K}$); and (c) YIG in contact with the YBCO CPW resonator, case C ($T = 30 \text{ K}$). The blue dashed lines display $\omega_{\text{FMR}}(H_0)$ [Eq. (1)] while the white dashed-dotted lines indicate the resonators' frequencies. The dotted lines in panels (b) and (c) correspond to the frequency of a broad mode due to the metal box hosting the CPW lines.

commutation relations. In the thermodynamic limit (i.e., $N \rightarrow \infty$), we can approximate $\hat{J}_+ \approx \sqrt{N} \hat{b}^\dagger$. Then, we obtain

$$\hat{\mathcal{H}} = \omega_c \hat{a}^\dagger \hat{a} + \omega_b \hat{b}^\dagger \hat{b} + \lambda(\hat{b} + \hat{b}^\dagger)(\hat{a} + \hat{a}^\dagger) + \beta(\hat{a} + \hat{a}^\dagger)^2, \quad (5)$$

which is the well-known Hopfield Hamiltonian [56].

We consider the dependence of the magnon resonance frequency ω_b on the external magnetic field H_0 as described by $\omega_b = \sqrt{\omega_H(\omega_H + \omega_M)} + \Delta$, leaving as the sole free parameter the energy shift Δ characterizing high-frequency magnons for the next step of our investigation. In our analysis we also leave as free parameters the cavity frequency ω_c , the collective coupling λ , and the factor of the diamagnetic term β .

The Hamiltonian in Eq. (3) can be expressed in terms of two noninteracting harmonic oscillators, $\hat{\mathcal{H}} = \Omega_- \hat{P}_-^\dagger \hat{P}_- + \Omega_+ \hat{P}_+^\dagger \hat{P}_+$, where \hat{P}_\pm are the polariton operators, which are linear combinations of light and matter operators, $\hat{P}_\mu = c_1^{(\mu)} \hat{a} + c_2^{(\mu)} \hat{b} + c_3^{(\mu)} \hat{a}^\dagger + c_4^{(\mu)} \hat{b}^\dagger$, with $\mu = \pm$. To fit our parameters, we need first to find the polariton frequencies, and, being a proper bosonic excitation of the system, the operator \hat{P}_μ fulfills the equation of motion of the harmonic oscillator, $[\hat{P}_\mu, \hat{\mathcal{H}}] = \Omega_\mu \hat{P}_\mu$. Since the polariton operator \hat{P}_μ is a linear combination of the light and matter operators, we need to calculate first the commutator of the latter with the Hamiltonian:

$$\begin{aligned} [\hat{a}, \hat{\mathcal{H}}] &= \omega_c \hat{a} + \lambda(\hat{b} + \hat{b}^\dagger), \\ [\hat{b}, \hat{\mathcal{H}}] &= \omega_b \hat{b} + \lambda(\hat{a} + \hat{a}^\dagger), \\ [\hat{a}^\dagger, \hat{\mathcal{H}}] &= -\omega_c \hat{a}^\dagger - \lambda(\hat{b} + \hat{b}^\dagger), \\ [\hat{b}^\dagger, \hat{\mathcal{H}}] &= -\omega_b \hat{b}^\dagger - \lambda(\hat{a} + \hat{a}^\dagger). \end{aligned}$$

The polariton frequencies Ω_μ are then obtained by finding the positive eigenvalues of the following Hopfield matrix:

$$\mathcal{M} = \begin{pmatrix} \omega_c + 2\beta & \lambda & -2\beta & -\lambda \\ \lambda & \omega_b & -\lambda & 0 \\ 2\beta & \lambda & -\omega_c - 2\beta & -\lambda \\ \lambda & 0 & -\lambda & -\omega_b \end{pmatrix}. \quad (6)$$

This leads to

$$\Omega_\pm = \frac{1}{\sqrt{2}} \sqrt{\tilde{\omega}_c^2 + \omega_b^2 \pm \sqrt{(\tilde{\omega}_c^2 - \omega_b^2)^2 + 16\omega_c\omega_b\lambda^2}}, \quad (7)$$

where $\tilde{\omega}_c = \sqrt{\omega_c(\omega_c + 4\beta)}$.

The above equation fits well the peaks of the S_{21} spectrum (case C). Figure 5 shows the best-fit result obtained with these parameters: $\omega_c/2\pi = 8.65 \text{ GHz}$, $\Delta/2\pi = 2.05 \text{ GHz}$, and $\lambda/2\pi = 2.002 \text{ GHz}$. For what concerns the diamagnetic parameter β , the only nontrivial result (i.e., nonzero result from the fit) has been obtained by assuming a dependence on the magnon frequency, $\beta = \alpha/\sqrt{\omega_b}$, which can be justified by the fact that the presence of this term is dominant at low frequencies. With this assumption, we obtained $\alpha/\sqrt{2\pi} = 3 \times 10^{-3} \text{ GHz}^{3/2}$, corresponding to a value of the diamagnetic coefficient $\beta/2\pi \sim 10^{-3} \text{ GHz}$ in the resonance condition. The ratio between the collective coupling and the cavity frequency is approximately 0.23, fulfilling the criterion $\lambda/\omega_c > 0.1$ for USC. The fit confirms that the influence of the diamagnetic term is almost negligible, leading us to conclude that the system couples to the resonator mainly through the spins. Notice that its value is more than two orders of magnitude smaller than the standard diamagnetic term for electric dipolar interactions (see Appendix D).

VII. DISCUSSION

The dispersion characteristics of the spin-wave spectrum in an infinite ferromagnetic film have been reported

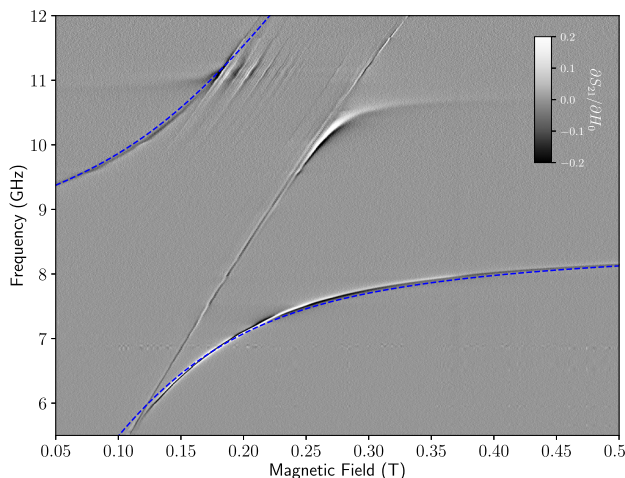


FIG. 5. Best fit of the transmission spectrum obtained in case C with the YIG film pressed on top of the superconducting YBCO CPW. The obtained parameters are: $\omega_c/2\pi = 8.65$ GHz, $\Delta/2\pi = 2.05$ GHz, $\lambda/2\pi = 2.002$ GHz, and $\alpha/\sqrt{2}\pi = 3 \times 10^{-3}$ GHz $^{3/2}$.

by Kalinikos and Slavin [57]. Taking into account both dipole-dipole and exchange interactions, theory predicts the excitation of perpendicular standing spin-wave (PSSW) modes even in the long-wave-number ($k_y d \ll 1$) limit. These modes are due to the broken translational invariance along the film thickness. Remarkably, in these conditions, the lowest mode shows a quasiuniform profile with a dispersion equation very similar to the Damon-Eshbach dipolar surface mode [Eq. (2)]. Conversely, higher-order PSSW modes display a nonuniform magnetization profile along z [57,58].

Broadband spectroscopy data in Fig. 3 evidence that the spin-wave spectrum is influenced by two main factors: (i) the distribution of the exciting electromagnetic field, and (ii) the boundary conditions at the ferrimagnet-superconductor interface. The effect of (i) emerges from the comparison between Figs. 3(a) and 3(b). In the case of the wide microstrip line, the modes calculated with Eqs. (1) and (2), the latter by considering $k = 2\pi/w'$ with $w' = 500$ μm , are very near. They both follow the measured dispersion of the lowest resonance mode in Fig. 3(a), showing that the magnetostatic approximation is valid in this case. Conversely, in the case of the narrow CPW line, the modes calculated with Eqs. (1) and (2) ($k = 2\pi/w$) are different. Since the main absorption line is found for $\omega(H_0) \approx \omega_{\text{DE}}(H_0)$ in Fig. 3(b), according to the dipole-exchange theory [57,58], we expect this mode to show a homogeneous magnetization profile along the film thickness.

The effect of (ii) is clearly evident from the direct comparison between Figs. 3(b) and 3(c), which shows the appearance of additional modes at $\omega > \omega_{\text{DE}}$ for superconductor and ferrimagnet in direct contact. The interplay

between a magnetically ordered film in the vicinity of a superconductor is an interesting and open issue. In the first instance, we can assume that the Meissner effect (perfect diamagnetism) imposes the expulsion of the oscillating field at the interface. Intuitively this can be visualized as a superconducting plane reflecting the image of the magnetic excitations in YIG [59,60]. Analysis of the portion of the spectrum can be attempted by simulations as suggested in Ref. [60], yet the dispersion law may depend to a large extent on the specific materials and geometry of the problem. We cannot exclude other mechanisms, like those related to vortex configuration and dynamics [40], anisotropy-induced surface pinning, and other interfacial effects [61], although these were reported for thin ferromagnetic films. Particular effects can also be induced on the superconductor, and these may depend on the type of superconducting wave function and on its coherence length. Whilst our experiments represent a case study involving insulating YIG and the high-critical-temperature YBCO superconductor that merits further attention, this issue goes beyond the scope of our research, which is focused on the ultrastrong-coupling regime, that can be achieved in different conditions and geometries.

In the experiments with YIG film and resonators [Fig. 4], the profile of the resonator field [Fig. 2] may introduce additional quantization of the spin-wave modes [62]. Consistently with Fig. 3(c), we note that the fitted value of the frequency shift $\Delta/2\pi = 2.05$ GHz is $\omega_{\text{DE}} < \Delta < \omega_M + \omega_H$, thus within the band of spin-wave resonance modes observed for YIG and YBCO CPW line in direct contact. This frequency shift can be reproduced by finite-element electromagnetic simulations [26], in which YIG film and resonator are respectively modeled as a gyrotropic medium and a perfect electric conductor (see Appendix A).

The collective coupling strength $\lambda/2\pi = 2.002$ GHz obtained by fitting the experimental data with Eq. (7) (Fig. 5) can be spelled out as $\lambda = g_s \sqrt{2s_{\text{Fe}}N}$, where $s_{\text{Fe}} = 5/2$ is the ground-state spin of YIG and $N = 1.8 \times 10^{15}$ is the total number of spins. The latter is much higher than the mean number of photons in the resonator [43,63]. The spin-photon coupling is $g_s = 21$ Hz as derived in Sec. III. Considering the spin density $\rho = 2 \times 10^{28} \text{ m}^{-3}$ [3] and the effective area of $4 \text{ mm} \times 45 \mu\text{m}$ in which the microwave field overlaps the YIG film [Figs. 2(a) and 2(b)], we can estimate an upper bound $d' \approx 500 \text{ nm} \ll d$ for the thickness of the portion of the YIG film coupled with the CPW resonator. This suggests that the magnon modes that are effectively coupled to the cavity one are located in close vicinity of the superconducting resonator. This observation is supported by similar experiments we performed with 20- μm -thick YIG film, which provide results quite similar to those obtained with the 5- μm -thick YIG film, thus confirming that the coupling is confined within few microns or less (Appendix B). The ratio between the collective couplings in configurations C and B is $g_{s,C}/g_{s,B}\sqrt{N_C/N_B} \approx 2$

[Figs. 4(b) and 4(c)]. From finite-element simulations, we estimated $g_{s,C}/g_{s,B} \approx 2$ due to the exponential decay of b_{vac} with z distance [Fig. 2(c)]. We therefore expect $N_C \approx N_B$. These observations indicate that, in our experiments, the achievement of the USC regime takes place mainly as a consequence of the optimized magnon-photon coupling strength.

The Hopfield model we used to analyze our spectra allows us to overcome the RWA generally used in previous works with magnetic systems, thus providing a quantum description of the problem that can be applied to safely explore the USC regime. We stress that the analysis of the spectrum reported in Sec. VI is quite robust since it relies on a minimal set of free parameters. Obviously, by introducing more degrees of freedom in the Hamiltonian, the spectrum can also be fitted well. For instance, one may wonder whether more magnetic modes couple to cavity photons simultaneously. Results of simulations with three (and more) modes are reported in Appendix C. It always results that the best fit is obtained with one dominant mode, ultrastrongly coupled to the resonator's one, plus additional modes coupled more weakly. As a matter of fact, on the basis of the sole fitting of the polaritonic branches, one cannot exclude that additional magnetic excitations are involved in our experiment and in similar ones reported in the literature. However, the representation with only one effective mode allows stringent bounds to be placed on the other terms of the Hamiltonian. Specifically, this is the case for the diamagnetic term, which in our analysis is vanishingly small. This result is consistent with what is expected for a pure spin interaction, although the issue is still debated in the literature. For instance, we just mention that conclusions reported in Ref. [36] lead to a finite diamagnetic contribution, yet, as those authors concluded, this may arise from surface plasmonic modes or by the different nature of magnetic material (permalloy). In our case, the absence of this diamagnetic term may be relevant for the observation of superradiant phase transition expected for $\lambda/\omega_c > 0.5$ (see discussion in Appendix D), making pure spin systems interesting and unique in this respect.

As concerns a possible route for applications, the coexistence of superconductivity and magnetism is not trivial since the presence of a magnetic field can be detrimental to the superconductor. In our experiments, the use of high-critical-temperature YBCO resonators, resilient to high magnetic field [39], indicates a good option for the realization of this kind of hybrid device. Our experiments also show that the contact between superconductor and magnet, and in particular the vanishing gap between the two, is critical to enhancing the coupling between magnetic and microwave modes [Fig. 4(b) and 4(c)]. The direct growth of YIG on top of superconducting oxide is not straightforward but there can be different options to overcome this technical issue [64,65]. The availability of

commercial YIG films of excellent quality allows the easy implementation of our experiment in different geometries.

VIII. CONCLUSIONS

In summary our results show a viable way to obtain the ultrastrong regime with a YIG film positioned in direct contact with a superconducting CPW resonator. The obtained collective coupling strength $\lambda/2\pi = 2.002$ GHz is improved by at least one order of magnitude with respect to previous reports involving YIG films in 3D cavities [66] or bulk YIG crystals in planar resonators [31,32]. The estimated λ/ω_c ratio of 0.23 and the cooperativity $C = 5 \times 10^4$ are among the largest reported so far for magnetic systems. Yet, we believe that there are still margins to further increase them, for instance by using planar resonators with more confined mode volumes and higher quality factors, or by means of YIG films detached from the GGG substrate [64,65] to reduce magnetic losses [67,68]. Finally, the very small diamagnetic coefficient (compared to standard electric dipole interactions) observed in these systems makes them suitable for exploring superradiant phase transitions [18–21].

ACKNOWLEDGMENTS

We thank Professor Bulat Rameev for useful discussions. This work was partially supported by the European Community through FET Open SUPERGALAX project (Grant Agreement No. 863313) and by the NATO Science for Peace and Security Programme (NATO SPS Project No. G5859). M.M. acknowledges TUBITAK-BIDEB for support under the 2219 scholarship program. S.S. acknowledges the Army Research Office (ARO) (Grant No. W911NF1910065).

APPENDIX A: ADDITIONAL FINITE-ELEMENT ELECTROMAGNETIC SIMULATIONS

We carried out electromagnetic simulations with commercial software (CST Microwave Studio) to evaluate the scattering parameters of the coupled system composed of CPW resonator and YIG film. The superconductor was modeled as a perfect electric conductor, whilst the magnetic film was included on the bottom face of the GGG substrate [69] with a thickness $d = 5 \mu\text{m}$.

Finite-element simulations were carried out by assuming that the precession of the magnetization in the ferrite can be described by the gyrotropic model, in which the permeability is modeled as a nonsymmetric Polder tensor with characteristic frequency dependence [12]. The magnetic dispersion of YIG was defined by directly introducing the Larmor frequency, $\omega_H/2\pi = \gamma\mu_0 H_0$, and the gyrotropic frequency, $\omega_M/2\pi = \gamma\mu_0 M_s$, as input parameters of the simulator, with $\gamma = 28.02 \text{ GHz/T}$, $\mu_0 = 4\pi \times 10^{-7} \text{ H/m}$, and $\mu_0 M_s = 0.245 \text{ T}$.

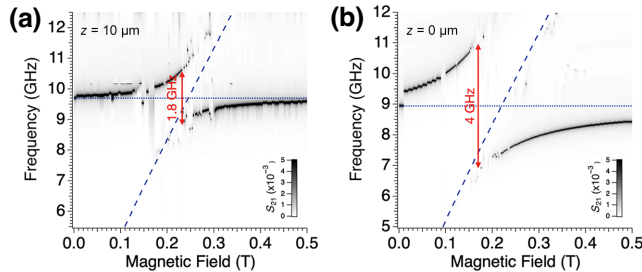


FIG. 6. Transmission spectral maps obtained by finite-element electromagnetic simulations. (a) The YIG film is lifted by 10 μm with respect to the surface of the CPW resonator. (b) The YIG film is in contact with the conducting surfaces of the resonator. Blue dashed lines indicate $\omega_{\text{FMR}}(H_0)$ while the dotted lines show ω_c in the two cases.

The simulation of frequency spectra was repeated for increasing values of the external magnetic field ($\mathbf{H}_0 = H_0 \hat{x}$) to obtain the spectral maps shown in Fig. 6. The evolution of the coupled YIG-resonator modes displays the appearance of polaritonic branches. The simulations carried out with the YIG film 10 μm above [panel (a)] or in contact with [panel (b)] the CPW resonator essentially reproduce the experimental trend shown in Figs. 4(b) and 4(c), showing a good correspondence with the measured splittings of the polaritonic branches. In agreement with the measured spectra, the spectral maps in Fig. 6 show that in both cases the lower polariton branch tends to $\omega_{\text{FMR}}(H_0)$ at low frequency. The increase of the splitting from panel (a) to (b) determines a shift of the anticrossing towards lower magnetic field, which is compatible with the frequency shift Δ introduced in Sec. VI.

For the sake of completeness, we mention that finite-element simulations fail to mimic the polariton line shapes shown in Ref. [43]. A more detailed model is probably required to reproduce broadening effects; however, this goes beyond the scope of our work.

APPENDIX B: EFFECTS OF YIG FILMS WITH DIFFERENT THICKNESS

Figure 7 shows a direct comparison between transmission data taken with the same CPW resonator and films of different thickness and size. In these experiments, the sample was held on the resonator with a copper spring; this resulted in a lower coupling with respect to data reported in the main body of the paper. Panel (a) shows the spectral map taken with the YIG/GGG film having a thickness of 5 μm and an area of approximately $4 \times 3 \text{ mm}^2$. Panel (b) shows data acquired on a YIG/GGG film having a thickness of 20 μm and area of approximately $5 \times 1 \text{ mm}^2$. The splitting indicated by the double-headed red arrow, corresponding to $2\lambda/2\pi \approx 3.6 \text{ GHz}$, is comparable in the two cases.

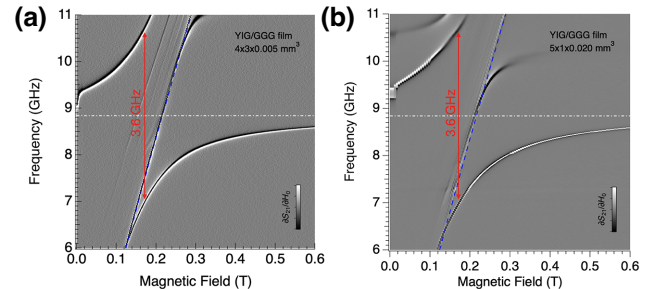


FIG. 7. Comparison between data obtained with YIG/GGG films of different thickness (at $T = 30 \text{ K}$): (a) 5 μm and (b) 20 μm . The red arrows indicate the splitting $2\lambda/2\pi \approx 3.6 \text{ GHz}$. The blue dashed lines display $\omega_{\text{FMR}}(H_0)$. Both measurements were carried out by means of the same YBCO CPW resonator. The horizontal dashed-dotted lines show the frequency of the fundamental mode in the two cases.

APPENDIX C: MULTIMODE FIT

Despite the fact that the fitting analysis presented in the main body of the paper involving one magnonic mode is statistically significant on its own, we extend the model by introducing more magnonic modes. In addition to the results shown in the main text, we present here the fitting results considering three magnonic modes (Fig. 8). The method can be straightforwardly extended from the case of a single mode, and the parameters obtained from the fit are: $\omega_c/2\pi = 8.64 \text{ GHz}$; $\Delta_0/2\pi = 0.23 \text{ GHz}$, $\Delta_1/2\pi = 1.92 \text{ GHz}$, and $\Delta_2/2\pi = 3.17 \text{ GHz}$; $\lambda_0/2\pi = 0.192 \text{ GHz}$, $\lambda_1/2\pi = 1.93 \text{ GHz}$, and $\lambda_2/2\pi = 0.2 \text{ GHz}$; and $\alpha/\sqrt{2\pi} = 0.035 \text{ GHz}^{3/2}$. Among the three modes, only one is ultrastrongly coupled with the cavity field. Again, the factor α of the diamagnetic term is very small.

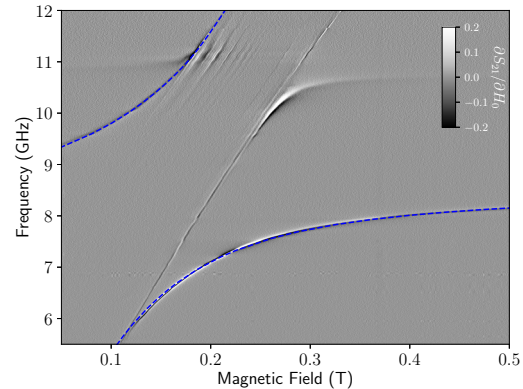


FIG. 8. Best fit of the transmission spectrum obtained in case C with the YIG film pressed on top of the superconducting YBCO CPW by considering three magnonic modes instead of only one: $\omega_c/2\pi = 8.64 \text{ GHz}$; $\Delta_0/2\pi = 0.23 \text{ GHz}$, $\Delta_1/2\pi = 1.92 \text{ GHz}$, and $\Delta_2/2\pi = 3.17 \text{ GHz}$; $\lambda_0/2\pi = 0.192 \text{ GHz}$, $\lambda_1/2\pi = 1.93 \text{ GHz}$, and $\lambda_2/2\pi = 0.2 \text{ GHz}$; and $\alpha/\sqrt{2\pi} = 0.035 \text{ GHz}^{3/2}$. Among the three modes, only one is ultrastrongly coupled with the cavity field. Again, the factor α of the diamagnetic term is very small.

0.2 GHz; and $\alpha/\sqrt{2\pi} = 0.035$ GHz $^{3/2}$. It is worth noting that, among the three modes, only one is found to be ultrastrongly coupled with the field of the resonator, corroborating the validity of considering only one magnonic mode. The obtained diamagnetic factor α is slightly larger than in the single-mode case.

APPENDIX D: ON THE DIAMAGNETIC TERM

It is useful to compare the obtained diamagnetic terms with the *standard* one, $\beta_{\text{std}} = \lambda^2/\omega_b$, which comes from the minimal coupling replacement [18,70] for electric dipolar interactions. Note that the expression for β_{std} is fixed by gauge-invariance requirements [70]. This constraint, preventing superradiance phase transitions, does not hold in the presence of magnetic interactions [18–21]. We calculate the ratio $\mathcal{B} \equiv \beta/\beta_{\text{std}} = \alpha\sqrt{\omega_b}/\lambda^2$, which gives $\mathcal{B} \approx 0.002$ and $\mathcal{B} \approx 0.027$ for the single-mode and three-mode cases, respectively. These results pave the way for the transition to a superradiant phase [18], as the obtained values are extremely low. To clarify the role of the diamagnetic term, Fig. 9 shows the polariton eigenfrequencies in three different conditions. Panel (a) shows the eigenfrequencies using the same parameters as in the fit obtained in the main text, which are: $\omega_c/2\pi = 8.65$ GHz, $\Delta/2\pi = 2.05$ GHz, $\lambda/2\pi = 2.002$ GHz, and $\alpha/\sqrt{2\pi} = 3 \times 10^{-3}$ GHz $^{3/2}$. The coupling strength is still too small to achieve a superradiant phase transition, but a slightly higher value would be enough to achieve it. Indeed, the continuous blue lines in panel (b) show the polariton eigenfrequencies in the absence of the diamagnetic term and a

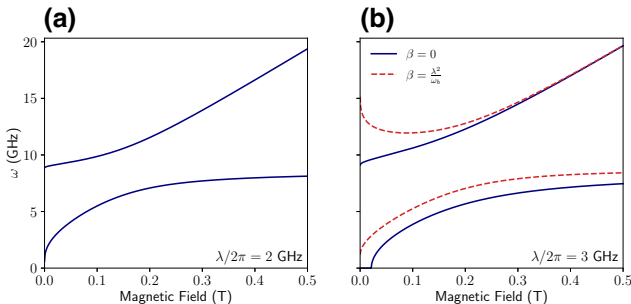


FIG. 9. (a) Polariton eigenfrequencies considering only one magnonic mode and using the same parameters as in the fit in the main text, which are: $\omega_c/2\pi = 8.65$ GHz, $\Delta/2\pi = 2.05$ GHz, $\lambda/2\pi = 2.002$ GHz, and $\alpha/\sqrt{2\pi} = 3 \times 10^{-3}$ GHz $^{3/2}$. Here the fitted term of the diamagnetic term is relatively small. However, the coupling λ is still too small to show the superradiant phase transition. (b) Polariton eigenfrequencies with the same parameters as before, except for $\lambda/2\pi = 3$ GHz, which is large enough to achieve the superradiant phase transition. The continuous blue lines correspond to the case of $\beta = 0$ (no diamagnetic term), clearly showing a critical point in the region of small magnetic fields. The red dashed lines correspond to $\beta = \lambda^2/\omega_b$, which avoids the superradiant phase transition.

larger coupling ($\beta = 0$ and $\lambda/2\pi = 3$ GHz). With these parameters, we can see a critical point in the region of small magnetic fields. On the other hand, as shown by the red dashed lines, the superradiant phase transition is forbidden by including the standard diamagnetic term of the Hopfield model ($\beta = \lambda^2/\omega_b$).

- [1] P. Pirro, V. I. Vasyuchka, A. A. Serga, and B. Hillebrands, Advances in coherent magnonics, *Nat. Rev. Mater.* **6**, 1114 (2021).
- [2] D. Lachance-Quirion, Y. Tabuchi, A. Gloppe, K. Usami, and Y. Nakamura, Hybrid quantum systems based on magnonics, *Appl. Phys. Express* **12**, 070101 (2019).
- [3] B. Zare Rameshti, S. Viola Kusminskiy, J. A. Haigh, K. Usami, D. Lachance-Quirion, Y. Nakamura, C.-M. Hu, H. X. Tang, G. E. Bauer, and Y. M. Blanter, Cavity magnonics, *Phys. Rep.* **979**, 1 (2022).
- [4] Y. Li, W. Zhang, V. Tyberkevych, W.-K. Kwok, A. Hoffmann, and V. Novosad, Hybrid magnonics: Physics, circuits, and applications for coherent information processing, *J. Appl. Phys.* **128**, 130902 (2020).
- [5] X. Zhang, C.-L. Zou, N. Zhu, F. Marquardt, L. Jiang, and H. X. Tang, Magnon dark modes and gradient memory, *Nat. Commun.* **6**, 8914 (2015).
- [6] L. Bai, M. Harder, P. Hyde, Z. Zhang, C.-M. Hu, Y. P. Chen, and J. Q. Xiao, Cavity Mediated Manipulation of Distant Spin Currents Using a Cavity-Magnon-Polariton, *Phys. Rev. Lett.* **118**, 217201 (2017).
- [7] N. Crescini, D. Alesini, C. Braggio, G. Carugno, D. Di Gioacchino, C. S. Gallo, U. Gambardella, C. Gatti, G. Iannone, G. Lamanna, C. Ligi, A. Lombardi, A. Ortolan, S. Pagano, R. Pengo, G. Ruoso, C. C. Speake, and L. Tafarello, Operation of a ferromagnetic axion haloscope at $m_a = 58$ μ eV, *Eur. Phys. J. C* **78**, 703 (2018).
- [8] R. Hisatomi, A. Osada, Y. Tabuchi, T. Ishikawa, A. Noguchi, R. Yamazaki, K. Usami, and Y. Nakamura, Bidirectional conversion between microwave and light via ferromagnetic magnons, *Phys. Rev. B* **93**, 174427 (2016).
- [9] B. Yao, Y. S. Gui, J. W. Rao, Y. H. Zhang, W. Lu, and C.-M. Hu, Coherent Microwave Emission of Gain-Driven Polaritons, *Phys. Rev. Lett.* **130**, 146702 (2023).
- [10] R. W. Roberts, B. A. Auld, and R. R. Schell, Magnetodynamic mode ferrite amplifier, *J. Appl. Phys.* **33**, 1267 (2004).
- [11] B. A. Auld, Coupling of electromagnetic and magnetostatic modes in ferrite loaded cavity resonators, *J. Appl. Phys.* **34**, 1629 (1963).
- [12] A. Gurevich and G. Melkov, *Magnetization Oscillations and Waves* (CRC Press, Boca Raton, Florida, 1996), 1st ed.
- [13] H. Maier-Flaig, S. Klingler, C. Dubs, O. Surzhenko, R. Gross, M. Weiler, H. Huebl, and S. T. B. Goennenwein, Temperature-dependent magnetic damping of yttrium iron garnet spheres, *Phys. Rev. B* **95**, 214423 (2017).
- [14] A. Imamoğlu, Cavity QED Based on Collective Magnetic Dipole Coupling: Spin Ensembles as Hybrid Two-Level Systems, *Phys. Rev. Lett.* **102**, 083602 (2009).

- [15] O. O. Soykal and M. E. Flatté, Strong Field Interactions Between a Nanomagnet and a Photonic Cavity, *Phys. Rev. Lett.* **104**, 077202 (2010).
- [16] A. Frisk Kockum, A. Miranowicz, S. De Liberato, S. Savasta, and F. Nori, Ultrastrong coupling between light and matter, *Nat. Rev. Phys.* **1**, 19 (2019).
- [17] P. Forn-Díaz, L. Lamata, E. Rico, J. Kono, and E. Solano, Ultrastrong coupling regimes of light-matter interaction, *Rev. Mod. Phys.* **91**, 025005 (2019).
- [18] P. Nataf and C. Ciuti, No-go theorem for superradiant quantum phase transitions in cavity QED and counter-example in circuit QED, *Nat. Commun.* **1**, 72 (2010).
- [19] G. Mazza and A. Georges, Superradiant Quantum Materials, *Phys. Rev. Lett.* **122**, 017401 (2019).
- [20] G. M. Andolina, F. M. D. Pellegrino, V. Giovannetti, A. H. MacDonald, and M. Polini, Theory of photon condensation in a spatially varying electromagnetic field, *Phys. Rev. B* **102**, 125137 (2020).
- [21] J. Román-Roche, F. Luis, and D. Zueco, Photon Condensation and Enhanced Magnetism in Cavity QED, *Phys. Rev. Lett.* **127**, 167201 (2021).
- [22] M. Goryachev, W. G. Farr, D. L. Creedon, Y. Fan, M. Kostylev, and M. E. Tobar, High-Cooperativity Cavity QED with Magnons at Microwave Frequencies, *Phys. Rev. Appl.* **2**, 054002 (2014).
- [23] J. Bourhill, N. Kostylev, M. Goryachev, D. L. Creedon, and M. E. Tobar, Ultrahigh cooperativity interactions between magnons and resonant photons in a YIG sphere, *Phys. Rev. B* **93**, 144420 (2016).
- [24] N. Kostylev, M. Goryachev, and M. E. Tobar, Superstrong coupling of a microwave cavity to yttrium iron garnet magnons, *Appl. Phys. Lett.* **108**, 062402 (2016).
- [25] B. Zare Rameshti, Y. Cao, and G. E. W. Bauer, Magnetic spheres in microwave cavities, *Phys. Rev. B* **91**, 214430 (2015).
- [26] G. Bourcin, J. Bourhill, V. Vlaminck, and V. Castel, Strong to ultrastrong coherent coupling measurements in a YIG/cavity system at room temperature, *Phys. Rev. B* **107**, 214423 (2023).
- [27] G. Flower, M. Goryachev, J. Bourhill, and M. E. Tobar, Experimental implementations of cavity-magnon systems: From ultra strong coupling to applications in precision measurement, *New J. Phys.* **21**, 095004 (2019).
- [28] L. Liensberger, A. Kamra, H. Maier-Flaig, S. Geprägs, A. Erb, S. T. B. Goennenwein, R. Gross, W. Belzig, H. Huebl, and M. Weiler, Exchange-Enhanced Ultrastrong Magnon-Magnon Coupling in a Compensated Ferrimagnet, *Phys. Rev. Lett.* **123**, 117204 (2019).
- [29] M. Bialek, J. Zhang, H. Yu, and J.-P. Ansermet, Strong Coupling of Antiferromagnetic Resonance with Subterahertz Cavity Fields, *Phys. Rev. Appl.* **15**, 044018 (2021).
- [30] J. R. Everts, G. G. G. King, N. J. Lambert, S. Kocsis, S. Rogge, and J. J. Longdell, Ultrastrong coupling between a microwave resonator and antiferromagnetic resonances of rare-earth ion spins, *Phys. Rev. B* **101**, 214414 (2020).
- [31] H. Huebl, C. W. Zollitsch, J. Lotze, F. Hocke, M. Greifenstein, A. Marx, R. Gross, and S. T. B. Goennenwein, High Cooperativity in Coupled Microwave Resonator Ferrimagnetic Insulator Hybrids, *Phys. Rev. Lett.* **111**, 127003 (2013).
- [32] R. G. E. Morris, A. F. van Loo, S. Kosen, and A. D. Karenowska, Strong coupling of magnons in a YIG sphere to photons in a planar superconducting resonator in the quantum limit, *Sci. Rep.* **7**, 11511 (2017).
- [33] J. T. Hou and L. Liu, Strong Coupling Between Microwave Photons and Nanomagnet Magnons, *Phys. Rev. Lett.* **123**, 107702 (2019).
- [34] I. A. Golovchanskiy, N. N. Abramov, V. S. Stolyarov, M. Weides, V. V. Ryazanov, A. A. Golubov, A. V. Ustinov, and M. Y. Kupriyanov, Ultrastrong photon-to-magnon coupling in multilayered heterostructures involving superconducting coherence via ferromagnetic layers, *Sci. Adv.* **7**, eabe8638 (2021).
- [35] Y. Li, V. G. Yefremenko, M. Lisovenko, C. Trevillian, T. Polakovic, T. W. Cecil, P. S. Barry, J. Pearson, R. Divan, V. Tyberkevych, C. L. Chang, U. Welp, W.-K. Kwok, and V. Novosad, Coherent Coupling of Two Remote Magnonic Resonators Mediated by Superconducting Circuits, *Phys. Rev. Lett.* **128**, 047701 (2022).
- [36] I. A. Golovchanskiy, N. N. Abramov, V. S. Stolyarov, A. A. Golubov, M. Y. Kupriyanov, V. V. Ryazanov, and A. V. Ustinov, Approaching Deep-Strong On-Chip Photon-to-Magnon Coupling, *Phys. Rev. Appl.* **16**, 034029 (2021).
- [37] R. Macêdo, R. C. Holland, P. G. Baity, L. J. McLellan, K. L. Livesey, R. L. Stamps, M. P. Weides, and D. A. Bozhko, Electromagnetic Approach to Cavity Spintronics, *Phys. Rev. Appl.* **15**, 024065 (2021).
- [38] S. Martínez-Losa del Rincón, I. Gimeno, J. Pérez-Bailón, V. Rollano, F. Luis, D. Zueco, and M. J. Martínez-Pérez, Measuring the Magnon-Photon Coupling in Shaped Ferromagnets: Tuning of the Resonance Frequency, *Phys. Rev. Appl.* **19**, 014002 (2023).
- [39] A. Ghirri, C. Bonizzoni, D. Gerace, S. Sanna, A. Cassinese, and M. Affronte, $\text{YBa}_2\text{Cu}_3\text{O}_7$ microwave resonators for strong collective coupling with spin ensembles, *Appl. Phys. Lett.* **106**, 184101 (2015).
- [40] B. Niedzielski, C. L. Jia, and J. Berakdar, Magnon-Fluxon Interaction in Coupled Superconductor/Ferromagnet Hybrid Periodic Structures, *Phys. Rev. Appl.* **19**, 024073 (2023).
- [41] C. Bonizzoni, M. Maksutoglu, A. Ghirri, J. van Tol, B. Rameev, and M. Affronte, Coupling sub-nanoliter BDPA organic radical spin ensembles with YBCO inverse anapole resonators, *Appl. Magn. Reson.* **54**, 143 (2022).
- [42] A. Ghirri, C. Herrero, S. Mazerat, T. Mallah, O. Moze, and M. Affronte, Coupling nanostructured CsNiCr Prussian blue analogue to resonant microwave fields, *Adv. Quantum Technol.* **3**, 1900101 (2020).
- [43] See Supplemental Material at <http://link.aps.org/supplemental/10.1103/PhysRevApplied.20.024039> for experimental details, additional transmission spectroscopy data and simulations.
- [44] G. Tosi, F. A. Mohiyaddin, H. Huebl, and A. Morello, Circuit-quantum electrodynamics with direct magnetic coupling to single-atom spin qubits in isotopically enriched ^{28}Si , *AIP Adv.* **4**, 087122 (2014).
- [45] C. Kittel, On the theory of ferromagnetic resonance absorption, *Phys. Rev.* **73**, 155 (1948).

- [46] C. Kittel, *Introduction to Solid State Physics* (Wiley, New York, 2004), 8th ed.
- [47] Y. Kajiwara, K. Harii, S. Takahashi, J. Ohe, K. Uchida, M. Mizuguchi, H. Umezawa, H. Kawai, K. Ando, K. Takanashi, S. Maekawa, and E. Saitoh, Transmission of electrical signals by spin-wave interconversion in a magnetic insulator, *Nature* **464**, 262 (2010).
- [48] I. S. Maksymov and M. Kostylev, Broadband stripline ferromagnetic resonance spectroscopy of ferromagnetic films, multilayers and nanostructures, *Phys. E: Low-Dimensional Syst. Nanostruct.* **69**, 253 (2015).
- [49] K. J. Kennewell, M. Kostylev, and R. L. Stamps, Calculation of spin wave mode response induced by a coplanar microwave line, *J. Appl. Phys.* **101**, 09D107 (2007).
- [50] L. Wang, Z. Lu, X. Zhao, W. Zhang, Y. Chen, Y. Tian, S. Yan, L. Bai, and M. Harder, Magnetization coupling in a YIG/GGG structure, *Phys. Rev. B* **102**, 144428 (2020).
- [51] M. Tsutsumi, T. Fukusako, and S. Yoshida, Propagation characteristics of the magnetostatic surface wave in the YBCO-YIG film-layered structure, *IEEE Trans. Microw. Theory Tech.* **44**, 1410 (1996).
- [52] D. Oates, A. Pique, K. Harshavardhan, J. Moses, F. Yang, and G. Dionne, Tunable YBCO resonators on YIG substrates, *IEEE Trans. Appl. Supercond.* **7**, 2338 (1997).
- [53] I. Diniz, S. Portolan, R. Ferreira, J. M. Gérard, P. Bertet, and A. Auffèves, Strongly coupling a cavity to inhomogeneous ensembles of emitters: Potential for long-lived solid-state quantum memories, *Phys. Rev. A* **84**, 063810 (2011).
- [54] A. Gherri, C. Bonizzoni, F. Troiani, N. Buccheri, L. Beverina, A. Cassinese, and M. Affronte, Coherently coupling distinct spin ensembles through a high- T_c superconducting resonator, *Phys. Rev. A* **93**, 063855 (2016).
- [55] T. Holstein and H. Primakoff, Field dependence of the intrinsic domain magnetization of a ferromagnet, *Phys. Rev.* **58**, 1098 (1940).
- [56] J. J. Hopfield, Theory of the contribution of excitons to the complex dielectric constant of crystals, *Phys. Rev.* **112**, 1555 (1958).
- [57] B. A. Kalinikos and A. N. Slavin, Theory of dipole-exchange spin wave spectrum for ferromagnetic films with mixed exchange boundary conditions, *J. Phys. C: Solid State Phys.* **19**, 7013 (1986).
- [58] S. O. Demokritov and A. N. Slavin, in *Handbook of Magnetism and Magnetic Materials*, edited by J. M. D. Coey and S. S. Parkin (Springer International Publishing, Cham, 2021), p. 281.
- [59] I. A. Golovchanskiy, N. N. Abramov, V. S. Stolyarov, V. V. Bolginov, V. V. Ryazanov, A. A. Golubov, and A. V. Ustinov, Ferromagnet/superconductor hybridization for magnonic applications, *Adv. Funct. Mater.* **28**, 1802375 (2018).
- [60] I. A. Golovchanskiy, N. N. Abramov, V. S. Stolyarov, V. V. Ryazanov, A. A. Golubov, and A. V. Ustinov, Modified dispersion law for spin waves coupled to a superconductor, *J. Appl. Phys.* **124**, 233903 (2018).
- [61] B. H. Lee, T. Fakhru, C. A. Ross, and G. S. D. Beach, Large Anomalous Frequency Shift in Perpendicular Standing Spin Wave Modes in biYIG Films Induced by Thin Metallic Overlays, *Phys. Rev. Lett.* **130**, 126703 (2023).
- [62] C. Bayer, J. Jorwick, S. O. Demokritov, A. N. Slavin, K. Y. Guslienko, D. V. Berkov, N. L. Gorn, M. P. Kostylev, and B. Hillebrands, in *Spin Dynamics in Confined Magnetic Structures III*, edited by B. Hillebrands and A. Thiaville (Springer Berlin Heidelberg, Berlin, Heidelberg, 2006), p. 57.
- [63] J. M. Sage, V. Bolkhovsky, W. D. Oliver, B. Turek, and P. B. Welander, Study of loss in superconducting coplanar waveguide resonators, *J. Appl. Phys.* **109**, 063915 (2011).
- [64] P. Trempler, R. Dreyer, P. Geyer, C. Hauser, G. Woltersdorf, and G. Schmidt, Integration and characterization of micron-sized YIG structures with very low Gilbert damping on arbitrary substrates, *Appl. Phys. Lett.* **117**, 232401 (2020).
- [65] S. Kosen, A. F. van Loo, D. A. Bozhko, L. Mihalceanu, and A. D. Karenowska, Microwave magnon damping in YIG films at millikelvin temperatures, *APL Mater.* **7**, 101120 (2019).
- [66] X. Zhang, C. Zou, L. Jiang, and H. X. Tang, Superstrong coupling of thin film magnetostatic waves with microwave cavity, *J. Appl. Phys.* **119**, 023905 (2016).
- [67] V. V. Danilov, D. L. Lyfar', Y. V. Lyubon'ko, A. Y. Nechiporuk, and S. M. Ryabchenko, Low-temperature ferromagnetic resonance in epitaxial garnet films on paramagnetic substrates, *Sov. Phys. J.* **32**, 276 (1989).
- [68] L. Mihalceanu, V. I. Vasyuchka, D. A. Bozhko, T. Langner, A. Y. Nechiporuk, V. F. Romanyuk, B. Hillebrands, and A. A. Serga, Temperature-dependent relaxation of dipole-exchange magnons in yttrium iron garnet films, *Phys. Rev. B* **97**, 214405 (2018).
- [69] D. A. Connolly, H. R. O. Aquino, M. Robbins, G. H. Bernstein, A. Orlov, W. Porod, and J. Chisum, Complex permittivity of gadolinium gallium garnet from 8.2 to 12.4 GHz, *IEEE Magn. Lett.* **12**, 1 (2021).
- [70] L. Garziano, A. Settineri, O. Di Stefano, S. Savasta, and F. Nori, Gauge invariance of the Dicke and Hopfield models, *Phys. Rev. A* **102**, 023718 (2020).